

AD-A060 457

TRW DEFENSE AND SPACE SYSTEMS GROUP REDONDO BEACH CALIF F/G 21/3  
PULSED PLASMA ACCELERATION IN STRONG BIAS MAGNETIC FIELDS FOR E--ETC(U)  
JUL 78 C L DAILEY, R H LOVBERG F44620-76-C-0107

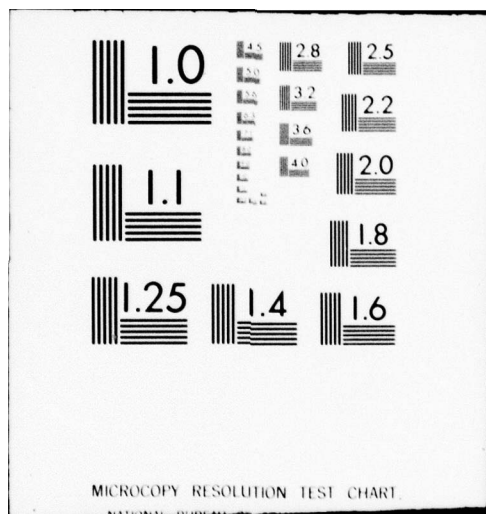
UNCLASSIFIED

AFOSR-TR-78-1408

NL

1 OF 1  
AD  
A060 457





19  
AFOSR-TR-78-1408

LEVEL II

18  
Contract No. F44620-76-C-0107  
15

2

AD A060457

6  
**PULSED PLASMA ACCELERATION IN  
STRONG BIAS MAGNETIC FIELDS  
FOR ELECTRIC PROPULSION  
APPLICATION.**

10 C.L. Dailey and R.H. Lovberg

16  
23/8

17 C1

DDC FILE COPY  
9  
July 31, 1978

11 31 Jul 78

12 46p.

Final Report, 1 Jun 76-31 May 78

DDC

RECEIVED  
OCT 30 1978

Prepared for  
AIR FORCE OFFICE OF SCIENTIFIC RESEARCH  
Bolling Air Force Base (Bldg. 410)  
Washington D.C. 20332

TRW DEFENSE AND SPACE SYSTEMS GROUP  
One Space Park, Redondo Beach  
California 90278

Approved for public release; distribution unlimited.

409 637  
10 16 123  
Approved for public release;  
distribution unlimited.  
mt

6

QUALIFIED requestors may obtain additional copies from the  
Defense Documentation Center, all others should apply to  
the National Technical Information Service.

AIR FORCE OFFICE OF SCIENTIFIC RESEARCH (AFSC)  
NOTICE OF TRANSMITTAL TO DDC  
This technical report has been reviewed and is  
approved for public release IAW AFR 190-12 (7b).  
Distribution is unlimited.  
A. D. BLOSE  
Technical Information Officer

#### CONDITIONS OF REPRODUCTION

Reproduction, translation, publication, use and disposal in whole or in part  
by or for the United States Government is permitted.



REPORT DOCUMENTATION PAGE		READ INSTRUCTIONS BEFORE COMPLETING FORM
1. REPORT NUMBER <b>AFOSR-TR- 78 - 1408</b>	2. GOVT ACCESSION NO.	3. RECIPIENT'S CATALOG NUMBER
4. TITLE (and Subtitle) <b>PULSED PLASMA ACCELERATION IN STRONG BIAS MAGNETIC FIELDS FOR ELECTRIC PROPULSION APPLICATION</b>	5. TYPE OF REPORT & PERIOD COVERED <b>FINAL</b> <b>1 June 1976 - 31 May 1978</b>	
	6. PERFORMING ORG. REPORT NUMBER	
7. AUTHOR(s) <b>C L DAILEY R H LOVBERG</b>	8. CONTRACT OR GRANT NUMBER(s) <b>F44620-76-C-0107</b>	
9. PERFORMING ORGANIZATION NAME AND ADDRESS <b>TRW DEFENSE AND SPACE SYSTEMS GROUP ONE SPACE PARK REDONDO BEACH, CA 90278</b>	10. PROGRAM ELEMENT, PROJECT, TASK AREA & WORK UNIT NUMBERS <b>2308C1 61102F</b>	
11. CONTROLLING OFFICE NAME AND ADDRESS <b>AIR FORCE OFFICE OF SCIENTIFIC RESEARCH/NA BLDG 410 BOLLING AIR FORCE BASE, D C 20332</b>	12. REPORT DATE <b>July 1978</b>	
	13. NUMBER OF PAGES <b>47</b>	
14. MONITORING AGENCY NAME & ADDRESS (if different from Controlling Office)	15. SECURITY CLASS. (of this report) <b>UNCLASSIFIED</b>	
15a. DECLASSIFICATION/DOWNGRADING SCHEDULE		
16. DISTRIBUTION STATEMENT (of this Report)  <b>Approved for public release; distribution unlimited.</b>		
17. DISTRIBUTION STATEMENT (of the abstract entered in Block 20, if different from Report)		
18. SUPPLEMENTARY NOTES		
19. KEY WORDS (Continue on reverse side if necessary and identify by block number) <b>PLASMA GENERATOR                      SPACE PROPULSION PLASMA ACCELERATOR                  SATELLITE POSITIONING AND MANEUVERING PULSED PLASMA THRUSTER BIAS FIELD THRUSTER ELECTRIC PROPULSION</b>		
20. ABSTRACT (Continue on reverse side if necessary and identify by block number) <b>It is shown that ohmic efficiency is limited to 50% for self-field quasi-steady plasma acceleration and for impulsive acceleration in small scale devices. This limit also applies when a constant bias field is added to the self-field but it can be removed by using a bias field that decreases in the acceleration direction. Tests were conducted with a bias field thruster in an attempt to demonstrate increased efficiency. It consisted of a V-shaped channel placed between pole pieces of a permanent magnet having the same divergence angle as the channel; electrodes were located in the upper and lower surfaces of the channel. Operation</b>		

was quasi-steady for a current discharge period of 800 microseconds. Gas injection was continuous and was done in two ways - in one mode it was introduced through hollow electrodes, in the other it entered the channel through a narrow slit. In the final version tested the channel was made of alumina and tungsten electrodes were used. Impulse enhancement due to the bias field was determined by suspending the magnet from piano wires and measuring its deflection when the thruster was fired. For argon injection through the electrodes, the current was carried downstream from the magnet in the usual self-field discharge mode and no magnet deflection occurred. For axial injection of argon a large magnet deflection occurred. However, this was found to be due to current carried on the sidewalls which was stabilized by the sidewalls and which produced severe ablation of the alumina. When a mixture of hydrogen and nitrogen was substituted for argon, no magnet deflection occurred, indicating the absence of wall current and presumably ablation. In this test a ceramic rod spanning the channel from one electrode to the other to stabilize the current in the magnet gap (flame holder) had no effect. It was concluded that impulse enhancement through the use of a bias magnetic field is not feasible.

UNCLASSIFIED

SECURITY CLASSIFICATION OF THIS PAGE(When Data Entered)

# FOREWORD

This program was sponsored by the Air Force Office of Scientific Research; Dr. B.T. Wolfson was Program Monitor. The work was done at TRW Defense and Space Systems Group by Dr. C.L. Dailey with Professor R.H. Lovberg of UCSD providing consulting assistance. Design and construction of the test equipment and much of the experimental work was carried out by W.P. Goldstein. The assistance of Ethel Johnson in readying this report for publication is appreciated.

ADDITION BY	
DTIC	DTIC Section <input checked="" type="checkbox"/>
DDI	DDI Section <input type="checkbox"/>
UNANNOUNCED	<input type="checkbox"/>
JUSTIFICATION	
BY	
DISTRIBUTION/AVAILABILITY CODES	
Dist.	AVAIL. and/or SPECIAL
A	



# CONTENTS

	Page
1. INTRODUCTION. . . . .	5
1.1 Relevance to Air Force Needs. . . . .	5
1.2 Magnetic Field Enhancement. . . . .	5
2. THEORETICAL BACKGROUND. . . . .	9
2.1 Constant Bias Field . . . . .	10
2.2 Decreasing Bias Field . . . . .	12
2.2.1 Dimensionless Formulation . . . . .	15
2.2.2 Effect of Accelerator Parameters on Ohmic Efficiency. . . . .	20
3. DESCRIPTION OF ACCELERATOR. . . . .	23
3.1 Channel . . . . .	23
3.2 Magnet. . . . .	24
3.3 Current Source. . . . .	27
4. EXPERIMENTAL METHODS. . . . .	31
4.1 Efficiency Measurements . . . . .	31
4.2 Diagnostic Measurements . . . . .	32
5. RESULTS . . . . .	33
6. CONCLUSIONS . . . . .	43

78 10 16 123

## ILLUSTRATIONS

		Page
1	Schematic Arrangement of Bias Field Thruster . . . . .	9
2	Relative Dissipation and Kinetic Power Densities (Constant E and B) . . . . .	12
3	Accelerator Channel Geometry for Decreasing Bias Field . . . . .	13
4	Effect of $R_N/M_A^2$ on Ohmic Efficiency. . . . .	19
5	Dimensionless Accelerator Parameters vs $R_N/M_A^2$ . . . . .	20
6	Effect of Magnet to Channel Gap Ratio on Efficiency at Two Values of $(R_N/M_A^2)_E$ ( $L/y_0 = 10$ , $\alpha = 20^\circ$ ). . . . .	21
7	Effect of Accelerator Length on Efficiency at Two Values of $(R_N/M_A^2)_E$ ( $y_{0B}/y_0 = 2$ , $\alpha = 20^\circ$ ). . . . .	21
8	Effect of Channel Wall Angle on Efficiency ( $y_{0B}/y_0 = 2$ , $L/y_0 = 10$ , $R_N/M_A^2 = 10$ ) . . . . .	22
9	Accelerator Channel. . . . .	23
10	Accelerator Channel Mounted on Vacuum Chamber. . . . .	24
11	Photograph of Ceramic Channel Showing Gas Manifold and Current Return Lead. . . . .	25
12	Demagnetization Curve for Brown-Bovari Samarium Cobalt Magnets . . . . .	26
13	Bias Field Magnet. . . . .	27
14	Magnetic Field at $\zeta$ for Different Magnet Configurations. . . . .	28
15	Variation of Magnetic Field Across Magnet Gap for Several Axial Stations . . . . .	29
16	Large Gap Magnet Used with Ceramic Channel . . . . .	29
17	Six-Section Pulse Line . . . . .	30
18	Current (upper trace) and Terminal Voltage (lower trace) for a Typical Discharge. . . . .	32
19	Lateral Variation of Axial Magnetic Field. . . . .	34
20	Axial Variation of Axial Magnetic Field at Side Wall . . . . .	34
21	Comparison of Magnet Impulse and Plasma Impulse Measurements . . . . .	35



# ILLUSTRATIONS (Continued)

	Page
22 Axial Variation of Current in Rogowsky Probe. . . . .	36
23 Glass Side-Wall Axial Injection Thruster Designed for Reduced Ablation. . . . .	37
24 Erosion of Copper Gas Inlet Electrode in Ceramic Mold . . . . .	38
25 Ablated Material on Inner Surfaces of Ceramic Model with Copper Gas Inlet/Electrodes. . . . .	39
26 Ablation in Ceramic Thruster with Tungsten Electrodes . . . . .	40
27 Tungsten Anode Ablation . . . . .	40
28 Ceramic Rod "Flame Holder" Before Testing . . . . .	41

## 1. INTRODUCTION

### 1.1 RELEVANCE TO AIR FORCE NEEDS

Low total impulse requirements for Air Force satellites are presently provided by small monopropellant rocket engines and resistojets. The growth in total impulse capability needed for the near future is being met by improving the useful lifetime of these engines. However, future satellites requiring much larger total impulse, either for attitude control and station keeping for long periods or for larger impulse maneuvers, such as orbit repositioning, will require the high specific impulse available with electric propulsion to avoid the unacceptable increases in propellant mass of the lower  $I_{sp}$  chemical thrusters. Development of the pulsed ablative, solid propellant thruster is proceeding for the relatively low impulse stationkeeping missions. To perform orbit repositioning with lighter weight than the chemical systems now in use, and to provide the capability for future requirements of multiple orbit shift maneuvers, a compact, lightweight, reliable electric thruster is needed. A pulsed electromagnetic thruster employing a strong bias magnetic field appeared to be a candidate for meeting this requirement with high efficiency.

### 1.2 MAGNETIC FIELD ENHANCEMENT

Plasma thrusters use the electromagnetic force developed by the plasma current in the local magnetic field to accelerate the plasma mass away from the thruster. In most cases the magnetic field is the resultant of the fields due to current flowing in the circuit and in the plasma, i.e., the "self-fields." For self-field accelerators, the current density at any point in the plasma is

$$j = \sigma(E - vB) \quad (1)$$

where  $\sigma$  is conductivity,  $v$  is plasma velocity, and  $E$  and  $B$  are electric and magnetic fields. The directions of  $v$ ,  $E$ , and  $B$  are mutually orthogonal and  $j$  is parallel to  $E$ .

Equation (1) can be rearranged to give

$$E = \frac{j}{\sigma} + vB \quad (2)$$

After multiplication by  $j$  this becomes

$$jE = \frac{j^2}{\sigma} + (jB)v \quad (3)$$

which expresses the input power density as the sum of the ohmic dissipation power density and the rate of mechanical work per unit volume done by the  $jB$  force density. If the only losses were ohmic, the efficiency would therefore be

or 
$$\eta = \frac{jB}{jBv + \frac{j^2}{\sigma}}$$

$$\eta = \frac{1}{1 + \frac{j}{\sigma Bv}} \quad (4)$$

For the simple case of a slab model with no bias field, with property variations in the acceleration direction only, the magnetic field gradient is approximately  $B/\delta$  where  $\delta$  is the interaction distance. Thus the Maxwell Curl - H relation is

$$j = \frac{1}{\mu} \frac{B}{\delta} \quad (5)$$

where  $\mu$  is the permeability of space, and Equation (4) can be written

$$\eta = \frac{1}{1 + \frac{1}{\mu\sigma\delta v}} \quad (6)$$



but since the diffusion speed of the magnetic field relative to the plasma is

$$v_d = \frac{1}{\mu\sigma\delta} \quad (7)$$

Equation (6) becomes

$$\eta = \frac{1}{1 + \frac{1}{R_N}} \quad (8)$$

where the magnetic Reynolds number  $R_N$  is the ratio of the plasma velocity to the diffusion speed. By multiplying the velocity terms by the acceleration time it is seen that the Reynolds number is also equal to the ratio of the acceleration distance to the field penetration depth,

$$R_N = \frac{v}{v_d} = \frac{\Delta}{\delta} \quad (9)$$

This ratio is large compared to unity for electromagnetic machines because the magnetic force is applied over a distance much larger than the dimension of the winding. This is also true for a metal plate accelerated impulsively by the rising current in a coil placed close to the plate, and for an exploding supernova.

For attitude control and station keeping of present satellites, the acceleration distance is comparable to the current sheet thickness so that the Reynolds number is nearly unity and the efficiency is limited to about 50% because of ohmic losses alone. Also for steady or quasi-steady plasma thrusters the current and magnetic field penetrate the plasma for the same distance over which acceleration occurs and the efficiency for such devices is also limited to 50%.

This limitation was recognized a few years ago during a study of impulsive plasma acceleration by inductive coupling between the plasma and circuit currents that was conducted by TRW Systems for the Air Force Office

of Scientific Research. An attempt was made at that time to increase the magnetic field in the interaction region through the use of inductively produced bias magnetic fields. The first experiment of this kind was successful. It used a pair of bias field coils whose axes were orthogonal to the accelerator coil axes so that the bias and accelerator circuits were decoupled. Attempts were then made to incorporate this principle in a practical thruster configuration by using coaxial bias and accelerator coils. Shorted turn shield coils were used to decouple the circuits. It was found that fields due to the current pulses in the shield coils effectively eliminated the bias fields at the time the plasma current was developed.<sup>1</sup>

The program described in this report was an attempt to avoid the limitation of the inductive bias field accelerator by using a permanent magnet to produce the bias field in an electrode thruster. It should be mentioned that a large scale impulsive thruster offers another way to get around the low Reynolds number limitation, provided "slug model" acceleration can be used to avoid the 50% impact heating loss that occurs in "snow plow model" acceleration. This may be feasible for future large scale satellites.

---

<sup>1</sup> Daily, C.L., H.A. Davis, and R.H. Lovberg, "Magnetic Field Annihilation of Impulsive Current Sheets," AFOSR-TR-76-0698, March 1976.



## 2. THEORETICAL BACKGROUND

The physical arrangement of the bias field thruster is indicated schematically in Figure 1. The plasma is accelerated in a V-shaped ceramic channel that is placed between the pole pieces of a permanent magnet. Current flows through the plasma between the upper and lower electrodes. The thruster operates in the quasi-steady mode with gas entering the channel through a narrow sonic slit and accelerating to a pressure less than 1 torr in the current carrying region. In addition to accelerating the gas, the divergent channel also serves to decrease the magnetic field in the acceleration direction. The reason for this can be seen by considering first the efficiency obtainable in a constant area channel.

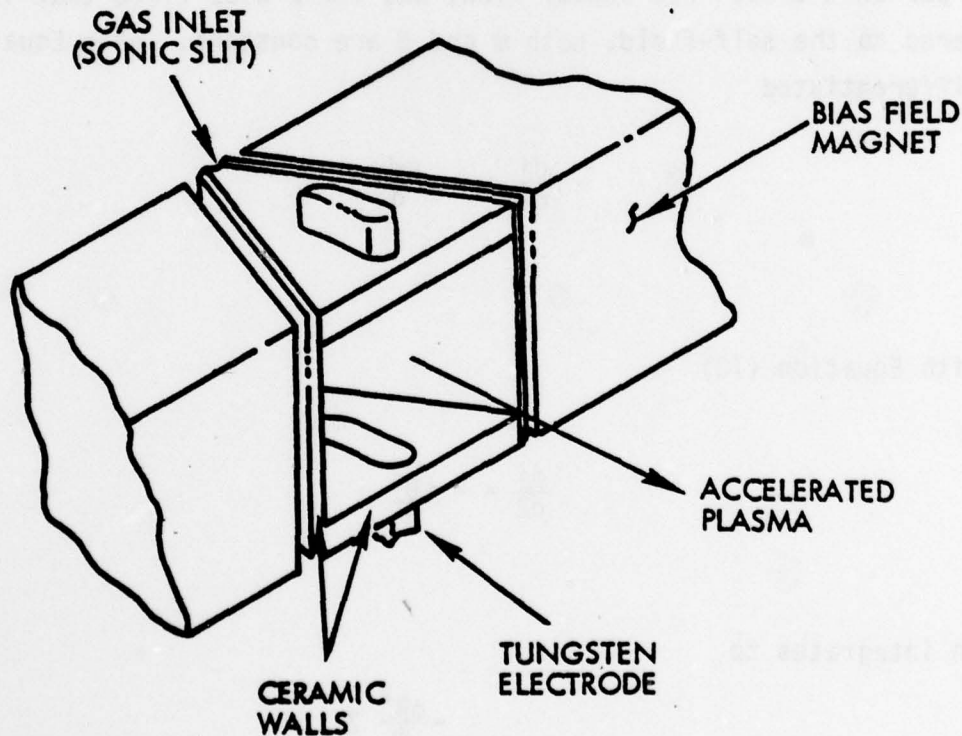


Figure 1. Schematic Arrangement of Bias Field Thruster

## 2.1 CONSTANT BIAS FIELD

It is interesting that the application of a bias field that is both spatially and temporally constant does not alter the ohmic efficiency. At any location in the accelerator

$$\rho v \frac{dv}{dz} = jB$$

or

$$\frac{dv}{dz} = \frac{jB}{\dot{m}} \quad (10)$$

where  $\rho$  is mass density,  $Z$  is the acceleration direction and  $\dot{m}$  is mass flow rate per unit area. For steady flow, and for a bias field that is large compared to the self-field, both  $\dot{m}$  and  $B$  are constant. When Equation (1) is differentiated

$$\frac{dj}{dz} = -\sigma B \frac{dv}{dz}$$

or with Equation (10)

$$\frac{dj}{dz} = -\frac{\sigma B^2}{\dot{m}} j$$

which integrates to

$$j = j_0 e^{-\frac{\sigma B^2}{\dot{m}} z} \quad (11)$$

This relation for the current density can be combined with Equation (10) to give

$$\frac{dv}{dz} = \frac{j_0 B}{m} e^{-\frac{\sigma B^2}{m} z}$$

which integrates to

$$v = \frac{j_0}{\sigma B} \left( 1 - e^{-\frac{\sigma B^2}{m} z} \right) \quad (12)$$

From Equation (11) the ohmic dissipation power density is

$$p = \frac{j^2}{\sigma} = \frac{j_0^2}{\sigma} e^{-\frac{2\sigma B^2}{m} z} \quad (13)$$

and by combining Equations (11) and (12) the kinetic power density is

$$p_k = jvB = \frac{j_0^2}{\sigma} \left( e^{-\frac{\sigma B^2}{m} z} - e^{-\frac{2\sigma B^2}{m} z} \right) \quad (14)$$

By integrating Equations (13) and (14) it is found that

$$\int_0^\infty p_D dz = \int_0^\infty p_k dz = \frac{j_0^2}{2\sigma B^2}$$

and the ohmic efficiency is 50% as it was for the self-field accelerator.



The variations with  $Z$  of the dissipative and kinetic power densities are shown in Figure 2. The former is a maximum at  $Z = 0$  and drops one e-fold by the time the kinetic power reaches its maximum. It is seen that not only  $B$ , but  $\sigma$  and  $\dot{m}$  have no effect on the 50% limit on efficiency. The e-fold distance is  $\sigma B^2/\dot{m}$  and increasing the bias field with all other variables held constant simply reduces the scale of the acceleration distance without affecting the efficiency.

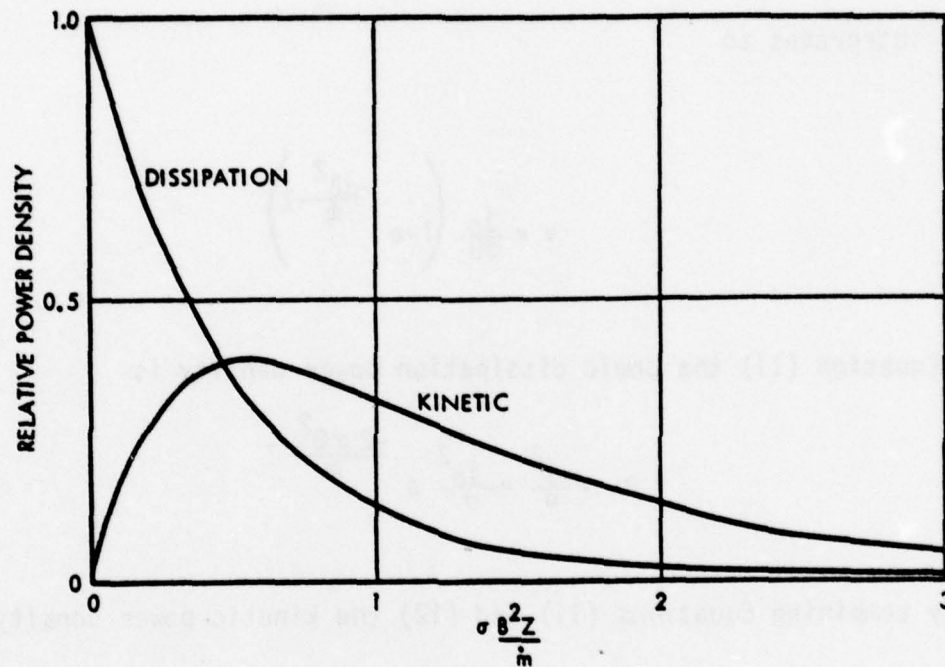


Figure 2. Relative Dissipation and Kinetic Power Densities (Constant  $E$  and  $B$ )

## 2.2 DECREASING BIAS FIELD

The ohmic efficiency limit of 50% is not inherent in the bias field concept but is a consequence of the bias field being held constant. It can be removed by using a field that decreases in the acceleration direction. The reason for this can be seen intuitively by referring to Equation (1). The current density (and hence the acceleration) drops to zero whenever

$v = E/B$ , i.e., when the back emf (in electric motor language) is equal to the applied electric field. This velocity (the plasma drift speed) is low when  $B$  is large. Thus by applying a large bias field near  $Z = 0$  the 50% limit on ohmic efficiency is reached when  $v$  is small, i.e., when both the kinetic and ohmic energies are low. The  $B$  field is then decreased, at constant  $E$ , so that  $E/B$  increases thereby increasing the kinetic energy.

This behavior can be examined in more detail by assuming that the bias field varies inversely as the local pole face separation. A linearly divergent channel is used, as illustrated in Figure 3.

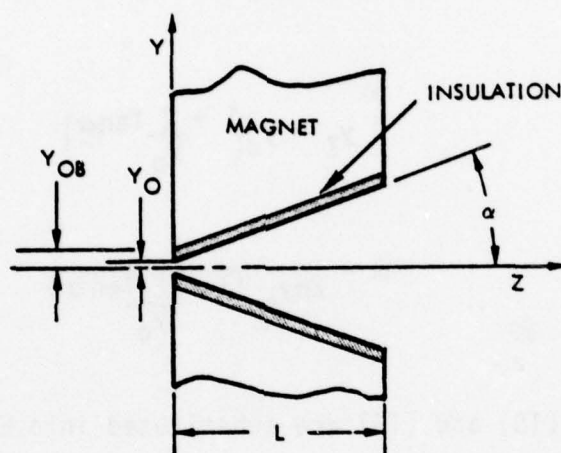


Figure 3. Accelerator Channel Geometry for Decreasing Bias Field

The distance from the centerline to the channel wall is  $y$  (at any  $Z$ ) and the distance to the magnet pole face is  $y_B$ . If  $B_0$  represents the field strength at  $Z = 0$ , then the value at any  $Z$  is

$$B = B_0 \frac{y_{0B}}{y_B}$$

but since

$$y_B = y_{0B} + Z \tan \alpha$$



it follows that

$$B = \frac{B_0}{1 + \frac{Z}{y_{0B}} \tan \alpha} \quad (15)$$

Another consequence of the divergent channel geometry is that  $\dot{m}$  is no longer constant. If  $\dot{M}$  represents the total mass flow rate and  $h$  is the channel height then

$$\dot{M} = 2hy\dot{m}$$

since

$$y_Z = y_0 \left( 1 + \frac{Z}{y_0} \tan \alpha \right)$$

$$\dot{m} = \frac{\dot{M}}{2hy_0 \left( 1 + \frac{Z}{y_0} \tan \alpha \right)} \quad (16)$$

When Equations (15) and (16) are substituted into Equation (10), the acceleration relation becomes

$$\frac{dv}{dZ} = \frac{2hy_0 B_0}{\dot{M}} \left( \frac{1 + \frac{Z}{y_0} \tan \alpha}{1 + \frac{Z}{y_{0B}} \tan \alpha} \right) j \quad (17)$$

Similarly the current density, from Equation (1), becomes

$$j = \sigma \left( E - \frac{vB_0}{1 + \frac{Z}{y_{0B}} \tan \alpha} \right) \quad (18)$$

The circuit current is the integral of the current density over the electrode length L,

$$I = 2 \int_0^L j y dZ = 2 y_0 \int_0^L \left(1 + \frac{Z}{y_0} \tan \alpha\right) j dZ \quad (19)$$

and the local plasma density is given by

$$\rho = \frac{\dot{M}}{2 y h v} = \frac{\dot{M}}{2 y_0 h v \left(1 + \frac{Z}{y_0} \tan \alpha\right)} \quad (20)$$

A numerical procedure can be used to calculate accerator efficiency by using Equation (18) to calculate  $j$  at an axial position  $Z$  where  $E$ ,  $B_0$  and  $v$  are known. Equation (17) then gives  $dv/dZ$  and the velocity at an adjacent downstream station becomes

$$v + \Delta v = v + \frac{dv}{dZ} \Delta Z \quad (21)$$

### 2.2.1 Dimensionless Formulation

If the current density from Equation (1) is substituted into Equation (10), the acceleration relation becomes

$$\frac{dv}{dZ} = \frac{\sigma B}{\rho v} (E - vB)$$

or

$$\frac{dv}{dZ} = \frac{\sigma B^2}{\rho \left(\frac{v}{E/B}\right)} \left(1 - \frac{v}{E/B}\right) \quad (22)$$

where  $E/B$  is the local drift speed. By making the initial value of  $B$  large (where the magnet gap is a minimum) the plasma speed approaches the drift speed in less than a millimeter. The remainder of the acceleration occurs with a small value for the difference term in Equation (22) multiplied by

a large coefficient. The magnitude of this coefficient increases with the conductivity, with the square of the local bias field and with decreasing local density. This illustrates how a large bias field can compensate for a low conductivity.

This point can be seen in a different way by completing the dimensionless formulation of Equation (22). Thus

$$\frac{d \frac{v}{E/B}}{d \frac{z}{L}} = \frac{\sigma L B^2}{\rho v} \left(1 - \frac{v}{E/B}\right) \quad (23)$$

where  $L$  is accelerator length, or since

$$\frac{\sigma L B^2}{\rho v} = \frac{\mu \sigma L v}{\left(\frac{v^2}{B^2}\right)} = \frac{R_N}{M_A^2}$$

it follows that

$$\frac{d \frac{v}{E/B}}{d \frac{z}{L}} = \frac{R_N}{M_A^2} \left(1 - \frac{v}{E/B}\right) \quad (24)$$

The Alfvén Mach number  $M_A$  is the ratio of the plasma velocity to the propagation speed of magnetic waves in the acceleration direction. By making this number small, through the use of a strong bias field, the effective Reynolds number is increased.

A more useful dimensionless formulation for calculation is to refer the velocity to the exit value of the drift speed rather than to the local value. Equation (23) then becomes

$$\frac{d \psi}{d \zeta} = \frac{2 y_E h L \sigma B_E^2}{\dot{M}} \left(1 - \psi \frac{B}{B_E}\right) \left(\frac{B}{B_E} \frac{y}{y_E}\right) \quad (25)$$



where

$$\psi = \frac{v}{E/B_E}$$

$$\zeta = \frac{Z}{L}$$

$$\frac{B}{B_E} = \frac{1 + \frac{L}{y_0 B} \tan \alpha}{1 + \zeta \frac{L}{y_0 B} \tan \alpha}$$

$$\frac{y}{y_E} = \frac{1 + \zeta \frac{L}{y_0} \tan \alpha}{1 + \frac{L}{y_0} \tan \alpha}$$

and

$$\frac{2y_E h L \sigma B_E^2}{\dot{M}} = \left( \frac{R_N}{M_A^2} \right)_E$$

The values for  $R_N$  and  $M_A$  are found after a calculation is finished and  $\psi_E$  has been determined. Thus the exit values of  $R_N$  and  $M_A$  are given by

$$R_{NE} = \mu \sigma L \left( \psi_E \frac{E}{B_E} \right)$$

$$M_{AE}^2 = \frac{\left( \psi_E \frac{E}{B_E} \right)^2}{\left( \frac{B_E^2}{\rho_E \mu} \right)} = \frac{\left( \psi_E \frac{E}{B_E} \right)}{2y_E h \left( \frac{B_E^2}{\mu \dot{M}} \right)} \quad (26)$$

From Equation (1) the dimensionless current density is

$$\frac{j}{\sigma E} = \left(1 - \psi \frac{B}{B_E}\right) \quad (27)$$

The circuit current is

$$I = \int 2y j dZ = 2y_0 L \sigma E \int_0^1 \left(\frac{j}{\sigma E}\right) \left(1 + \zeta \frac{L}{y_0} \tan \alpha\right) d\zeta$$

or in dimensionless form

$$\frac{I}{2y_0 L \sigma E} = \int_0^1 \frac{j}{\sigma E} \left(1 + \zeta \frac{L}{y_0} \tan \alpha\right) d\zeta \quad (28)$$

The input power is

$$W = IV = 2y_0 h L \sigma E^2 \int_0^1 \left(\frac{j}{\sigma E}\right) \left(1 + \zeta \frac{L}{y_0} \tan \alpha\right) d\zeta$$

and the ohmic loss is

$$\Omega = \int \frac{2yh}{\sigma} j^2 dZ = 2y_0 h L \sigma E^2 \int_0^1 \left(\frac{j}{\sigma E}\right)^2 \left(1 + \zeta \frac{L}{y_0} \tan \alpha\right) d\zeta$$

The ohmic efficiency is therefore

$$\eta = 1 - \frac{\Omega}{W} = 1 - \frac{\int_0^1 \left(\frac{j}{\sigma E}\right)^2 \left(1 + \zeta \frac{L}{y_0} \tan \alpha\right) d\zeta}{\int_0^1 \left(\frac{j}{\sigma E}\right) \left(1 + \zeta \frac{L}{y_0} \tan \alpha\right) d\zeta} \quad (29)$$

From Equation (29) a qualitative estimate of the efficiency is

$$\eta = 1 - \frac{j}{\sigma E} = \frac{V}{E/B}$$



or, from Equation (24)

$$\frac{dn}{d\zeta} = \frac{R_N}{M_A^2} (1 - n)$$

After integration this becomes

$$n = 1 - e^{-\frac{R_N}{M_A^2} \zeta} \quad (30)$$

A plot of this relation is shown in Figure 4. The efficiency is over-estimated but the importance of the Reynolds number parameter is correctly illustrated.

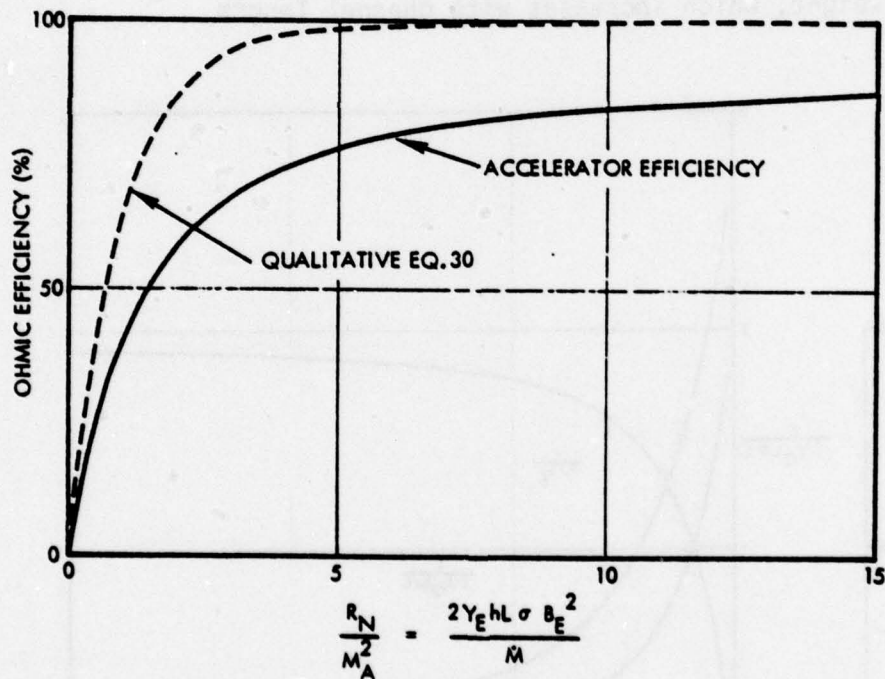


Figure 4. Effect of  $R_N/M_A^2$  on Ohmic Efficiency

$$\left( \frac{y_{0B}}{y_0} = 2, \frac{L}{y_0} = 10, \alpha = 20^\circ \right)$$

### 2.2.2 Effect of Accelerator Parameters on Ohmic Efficiency

Figure 4 shows the effect of the parameter  $R_N/M_A^2$  on ohmic efficiency for the geometric parameters  $y_{0B}/y_0 = 2$ ,  $L/y_0 = 10$  and  $\alpha = 20^\circ$ . At a value of 1.0 the efficiency is 40%, which agrees well with the self-field accelerator estimate. At a value of 10 the efficiency has increased to 84%. The corresponding accelerator parameters are plotted in Figure 5.

The effects on efficiency of the magnet to channel gap ratio, the channel length to gap ratio and the channel wall angle are shown in Figures 6 through 8, respectively. From Figure 6 it is seen that the gap ratio should be as small as possible for maximum efficiency. This means that the insulating walls separating the magnet pole faces from the plasma should be as thin as possible. Figure 7 shows that the channel length should be about 10 times the gap dimension.

The optimum length would require a tradeoff between efficiency and magnet weight, which increases with channel length.

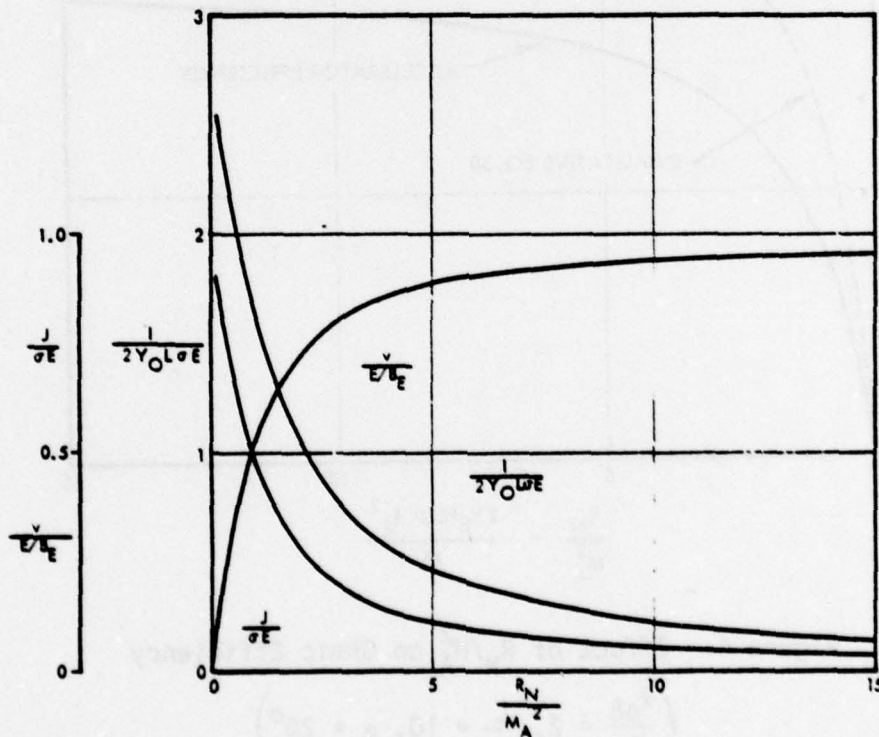


Figure 5. Dimensionless Accelerator Parameters vs  $R_N/M_A^2$

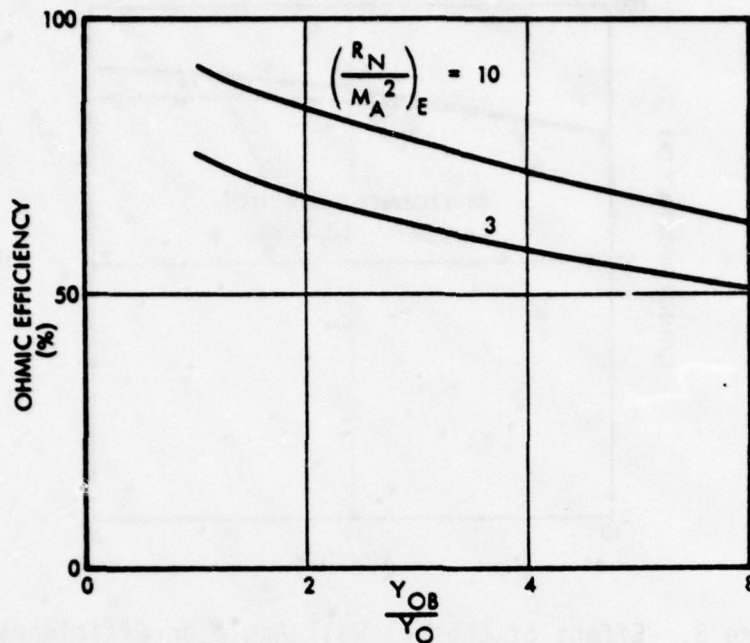


Figure 6. Effect of Magnet to Channel Gap Ratio on Efficiency at Two Values of  $(\frac{R_N}{M_A^2})_E$  ( $L/y_0 \approx 10$ ,  $\alpha = 20^\circ$ )

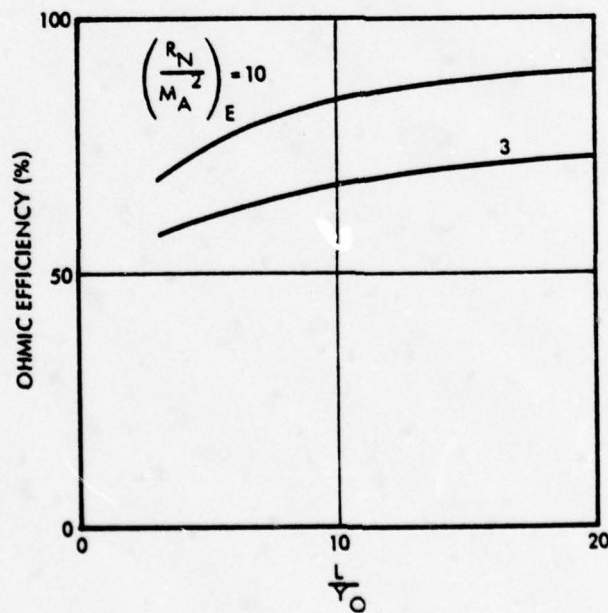


Figure 7. Effect of Accelerator Length on Efficiency at Two Values of  $(\frac{R_N}{M_A^2})_E$  ( $y_{OB}/y_0 = 2$ ,  $\alpha = 20^\circ$ )

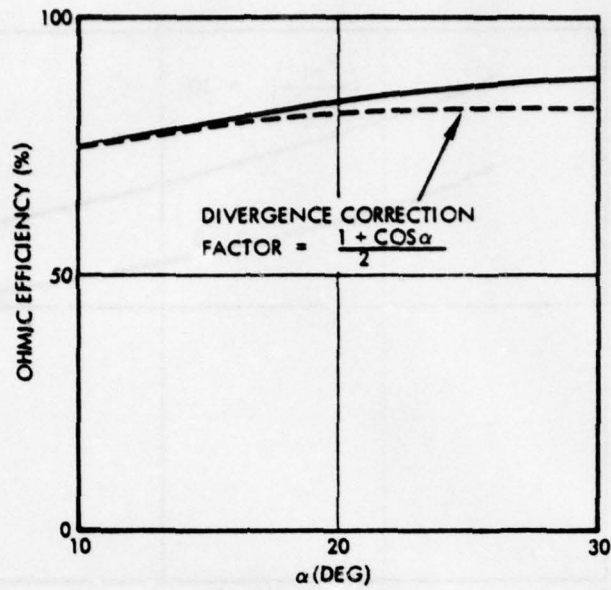


Figure 8. Effect of Channel Wall Angle on Efficiency  
 $(y_{oB}/y_o = 2, L/y_o = 10, R_N/M_A^2 = 10)$



### 3. DESCRIPTION OF ACCELERATOR

#### 3.1 CHANNEL

Several accelerator channels were tested during the program in an attempt to decrease the amount of insulator ablation that was added to the plasma during the discharge. The initial channel is shown in Figure 9. It was mounted to a lucite plate on one of the ports of a 4 x 8 foot vacuum chamber as shown in Figure 10.

The electrodes of the channel shown in Figure 9 were made of 1/4-inch thick brass while 1/16-inch thick glass plates were used for the side walls. Gas was admitted to the acceleration region through a sonic slit about 1/4 mm wide. The electrode separation was 2.5 cm. The electrode length in the flow direction was 3.2 cm for the first device tested. This was later shortened to 1.3 cm by covering the downstream portions with glass plates. The last channel tested is shown in Figure 11. It had tungsten electrodes and all four of the channel surfaces were made of high purity alumina. The edges where the surfaces joined were recessed such that the RTV used for the vacuum seal, seen in Figure 11, was not exposed to the

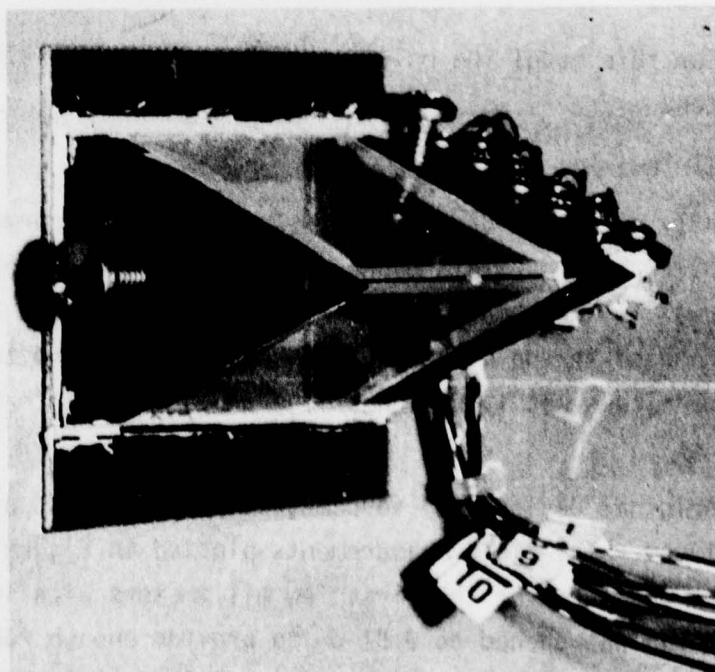


Figure 9. Accelerator Channel

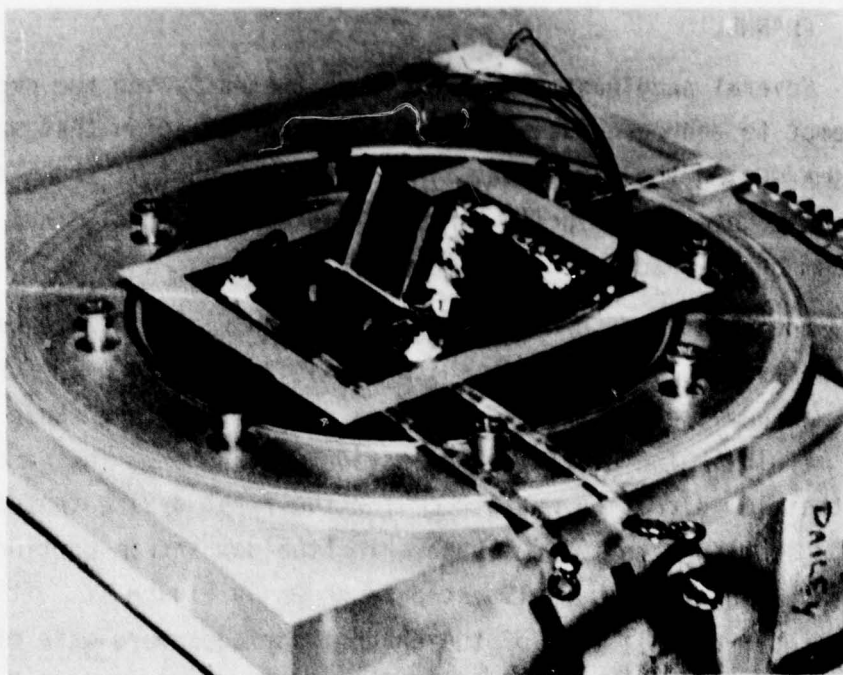


Figure 10. Accelerator Channel Mounted on Vacuum Chamber

plasma. For this model the only materials subject to ablation were alumina and tungsten.

### 3.2 MAGNET

Recently developed Brown-Bovari samarium-cobalt permanent magnets were used to drive the bias field magnetic circuit. A demagnetization curve for this material is shown in Figure 12. As shown in Figure 12, eight magnet blocks were used in the structure (four in parallel and two in series). Each of the blocks was 1.25 inches long and had a 1-inch square cross section.

The original design used four magnetic blocks with a minimum gap spacing of 0.19 cm. The field measurements plotted in Figure 14 show that high fields were obtained for the first few millimeters with low values near the exit. The gap was opened to 0.51 cm to provide enough room for the glass side walls so that the apex of the plasma volume would be near the leading edge of the pole pieces. Field strength plots are shown in Figure 14 for

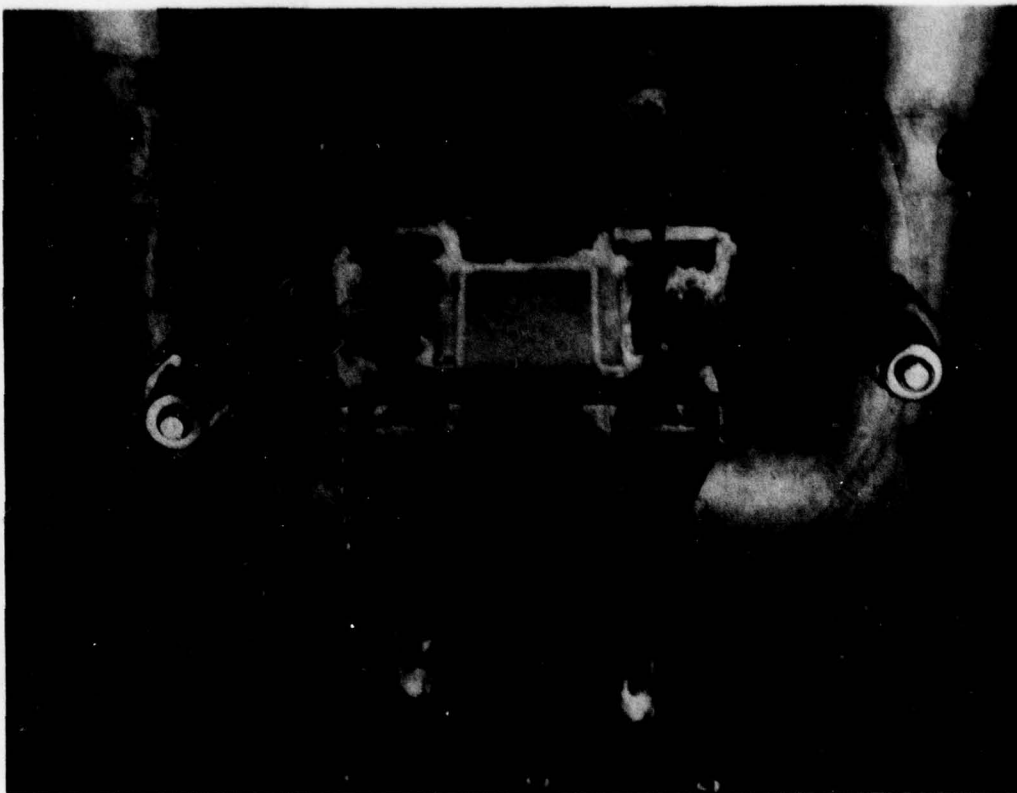


Figure 11. Photograph of Ceramic Channel Showing Gas Manifold and Current Return Lead

four, six, and eight magnet blocks. The latter configuration was used for most of the experiments. As shown in the figure, the field along the axis is prescribed reasonably well represented by the relation

$$B_y = \frac{0.954}{1 + \frac{2z \tan 22.5^\circ}{0.51}}$$

The lateral variation of the magnetic field across the gap was measured at several positions to determine the uniformity of the field at a given axial station. The results, plotted in Figure 15, show that the variation was reasonably small.

For the last series of tests conducted during the program, those conducted with the ceramic accelerator channel shown in Figure 11, the eight magnet blocks were remounted in the pole pieces shown in Figure 16. For this magnet, the narrow end gap was increased to 0.35 inch and the length of the pole face (in the acceleration direction) was reduced to 0.7 inch.



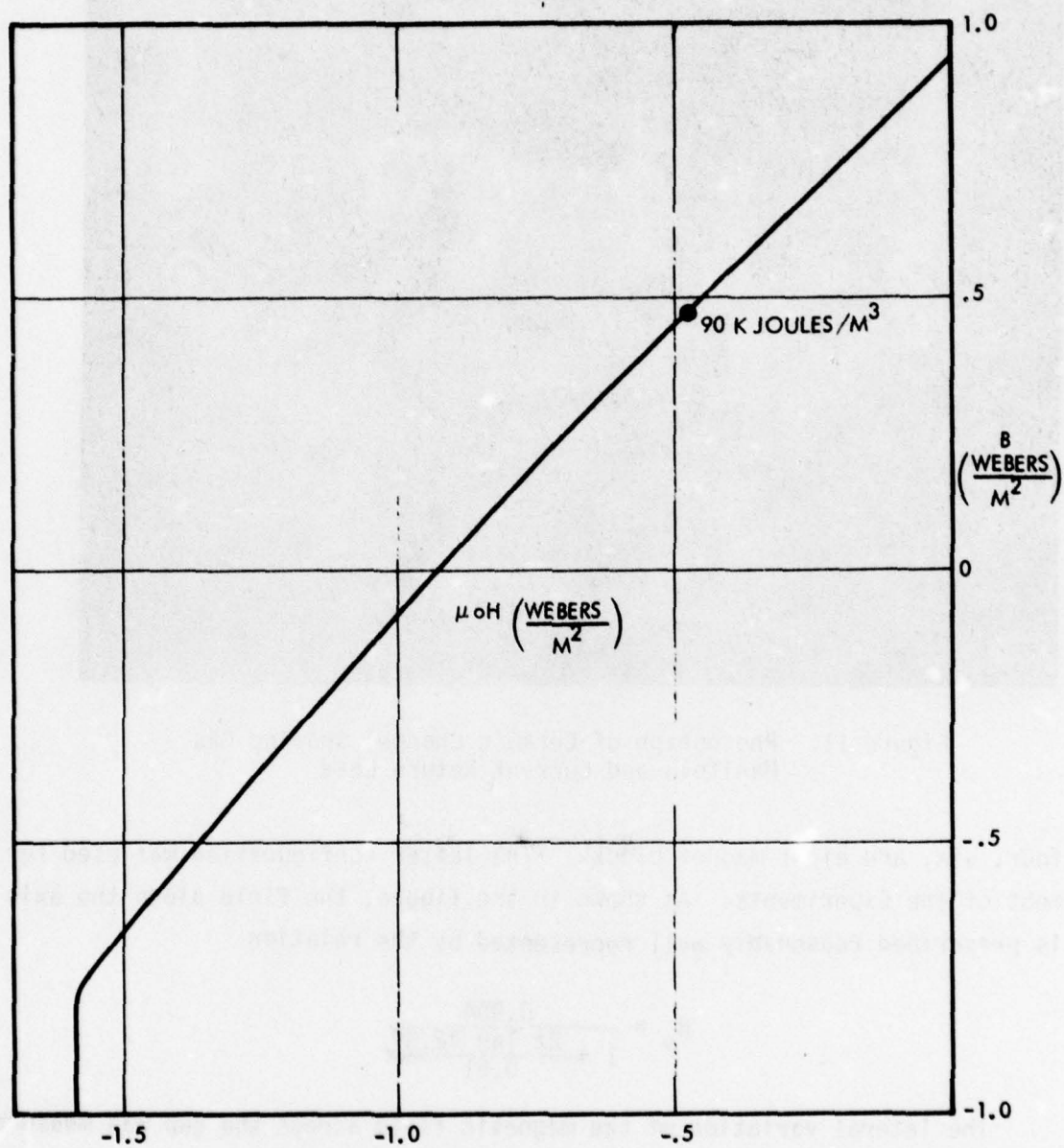


Figure 12. Demagnetization Curve for Brown-Bovari Samarium Cobalt Magnets



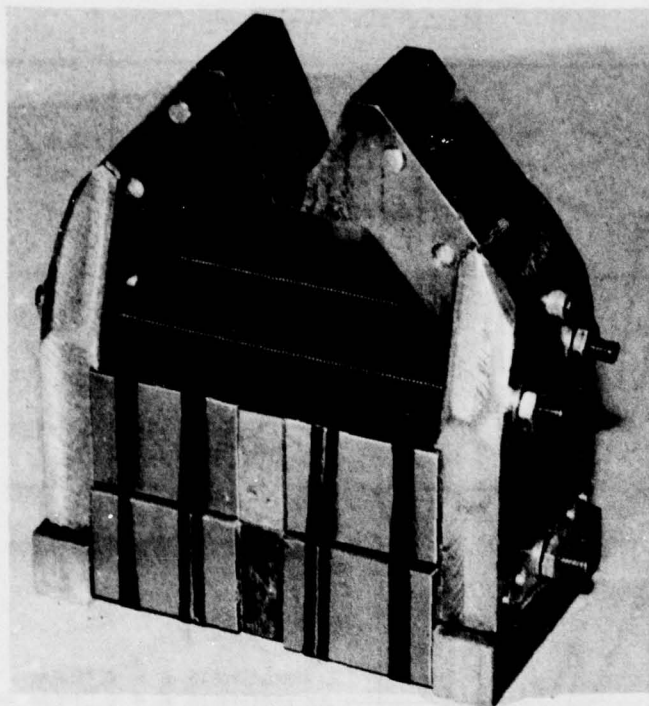


Figure 13. Bias Field Magnet

This moved the magnet forward relative to the electrodes so as to increase the bias field in the plasma current region.

### 3.3 CURRENT SOURCE

Current for the discharge was supplied by the six element pulse line shown in Figure 17. Each section of the line had 780  $\mu\text{F}$  capacitance and 6  $\mu\text{H}$  inductance. The total capacitance of the electrolytic capacitors was 4800  $\mu\text{F}$  and the pulse duration of the line was

$$\tau = 2 \sqrt{LC} = 820 \mu \text{ sec}$$

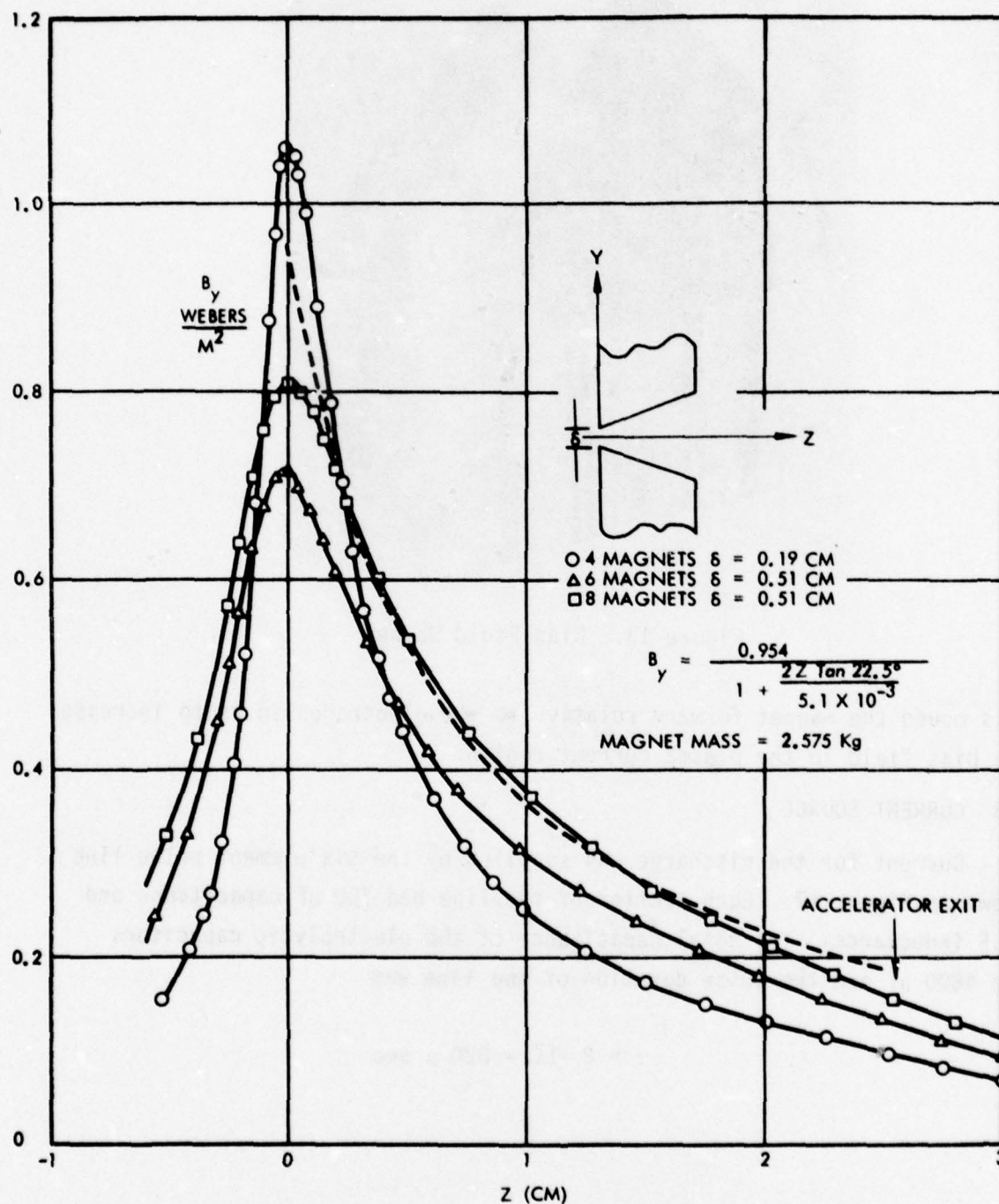


Figure 14. Magnetic Field at Q for Different Magnet Configurations

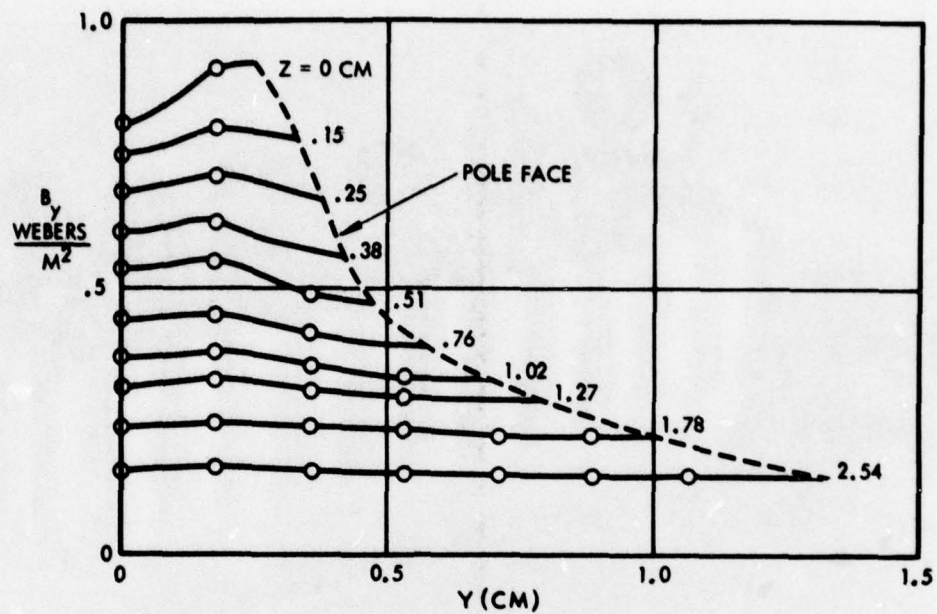


Figure 15. Variation of Magnetic Field Across Magnet Gap for Several Axial Stations (eight magnets,  $\delta = 0.51$  cm)

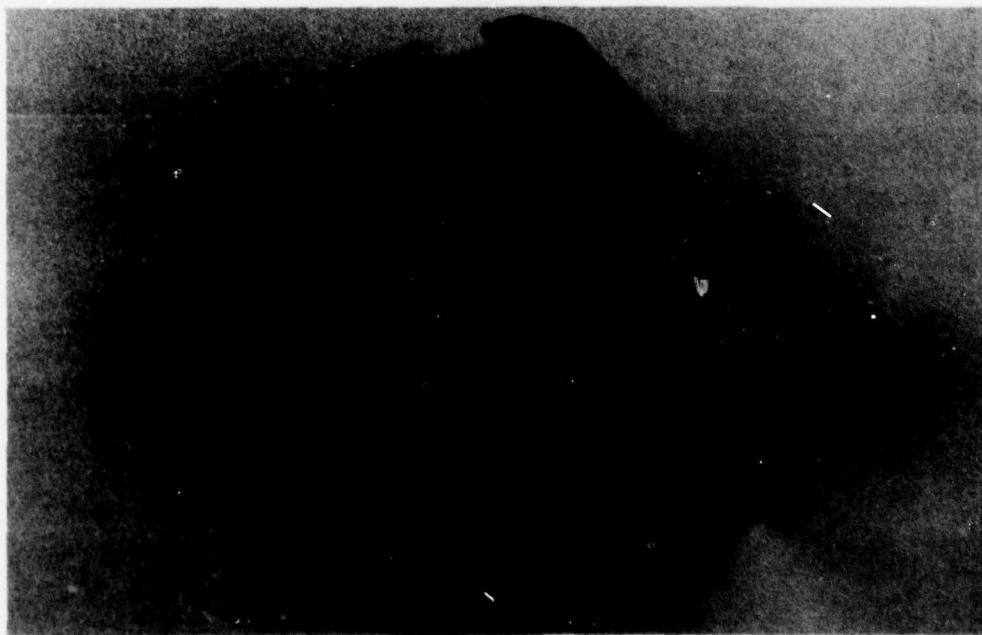


Figure 16. Large Gap Magnet Used with Ceramic Channel



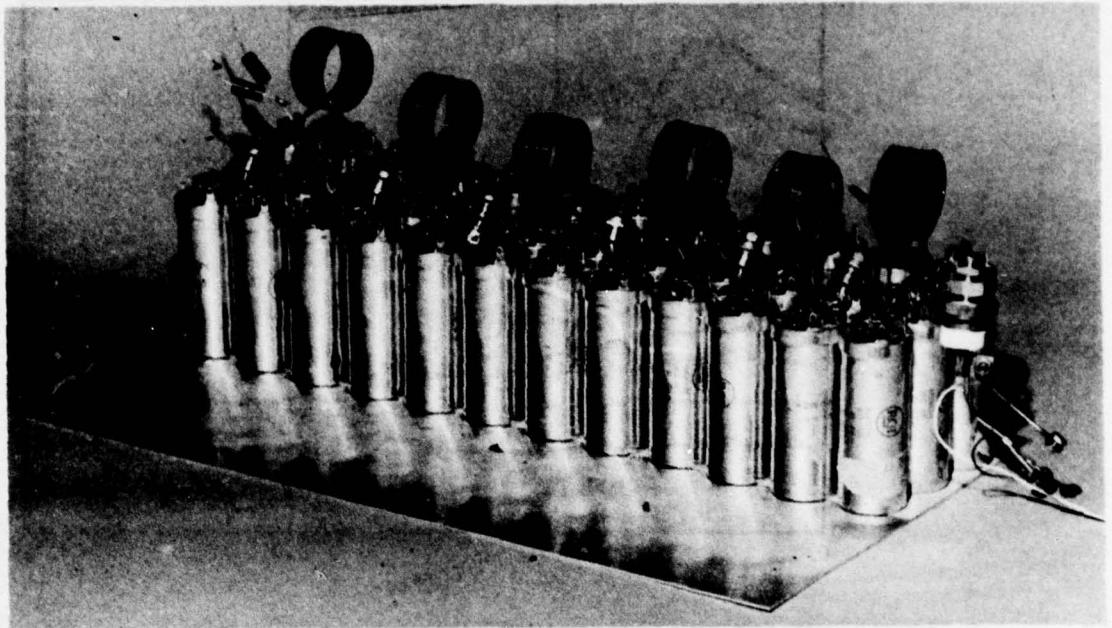


Figure 17. Six-Section Pulse Line



## 4. EXPERIMENTAL METHODS

### 4.1 EFFICIENCY MEASUREMENT

The experimental efficiency was found from the relation

$$\eta = \frac{MV^2}{2J} = \frac{MVgI_{sp}}{2J}$$

or

$$\eta = \frac{\Delta I g I_{sp}}{2J} \quad (32)$$

where  $\Delta I$  is the impulse per shot,  $M$  is propellant ejected per shot and  $J$  is the product of voltage and current at the electrode terminals integrated over the discharge period. The  $I_{sp}$  was found from the relation

$$I_{sp} = \frac{\Delta I}{Mg} \quad (33)$$

The mass flow rate into the thruster was calculated using the measured fillup rate of the vacuum chamber at constant supply pressure.

The impulse bit  $\Delta I$  was determined by suspending the magnet structure from a pair of 1.4 meter long piano wires and measuring its deflection when the thruster was fired; the deflection was of the order of 2 mm and could be read with a repeatability of  $\pm 5\%$  by using a microscope.

The impulse measured in this way included only the electromagnetic force arising from the interaction of the plasma current with the bias field; it did not include the impulse due to the self-field acceleration. Thus zero magnet deflection would indicate no gain in efficiency relative to a self-field accelerator, rather than zero thruster efficiency.

An independent measurement of total impulse was made by collecting the accelerated plasma in a 12-inch diameter by 16-inch long cylinder of aluminum foil suspended from threads inside the vacuum chamber. Four threads were used, attached to a lightweight frame to which the cylinder was mounted. This method of suspension minimized the oscillations that were induced by the high velocity gas flow through the accelerator before the capacitor bank was discharged. The data reading technique was first to

observe the position of a pointer attached to the cylinder relative to a meter stick in the vacuum chamber with no gas flow, then to estimate the maximum deflection in the gas stream before and after the discharge. From the known geometry of the suspension the increase in potential energy of the pendulum was calculated.

The input energy in the denominator of Equation (33) was measured by integrating the product of the circuit current and the voltage across the electrodes for each test condition. A typical oscillograph record is shown in Figure 18. A pair of voltage probes and a differential amplifier were used for the voltage data while the voltage drop across a low impedance series resistor ( $0.167\text{ m}\Omega$ ) was used to measure current. The accelerator impedance for this case is seen to be about  $50\text{ m}\Omega$ .

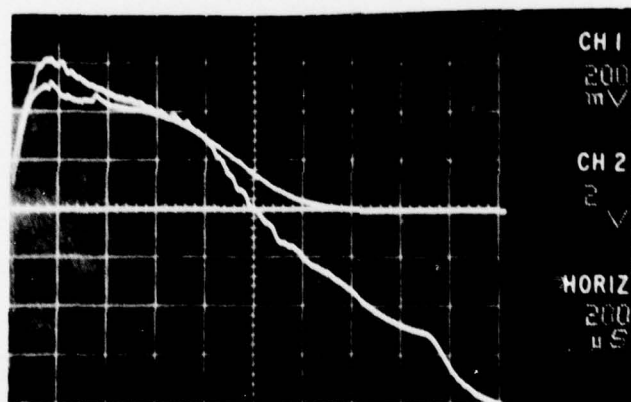


Figure 18. Current (Upper Trace) and Terminal Voltage (Lower Trace) for a Typical Discharge (20 V/cm, 1200 A/cm)

#### 4.2 DIAGNOSTIC MEASUREMENTS

Measurements of current and magnetic fields in the plasma were made with miniature probes. Because of the small size of the thruster it was not feasible to obtain meaningful spatial distribution of these properties. The measurements however were helpful in locating the current, i.e., in determining the principal features of the discharge.

## 5. RESULTS

As can be seen from Equation (32) the ratio of  $\eta$  to  $I_{sp}$  is independent of the mass accelerated and depends only on measurements of  $\Delta I$  and  $J$ . Measurements with the first accelerator tested (Figure 9) gave  $I_{sp}$  values calculated from Equation (33) that led to efficiencies from Equation (32) well over 100%. There appeared to be two possible explanations. One was that the current ran partly along the glass sidewall and the other was that additional mass was added by ablation. If current were running on the sidewall it would produce a large force on the magnet without exerting a comparable force on the plasma because of wall friction. To examine this possibility the lateral distribution of the axial magnetic field was measured midway between the electrodes. If this variation were monotonic it would indicate current flow on the sidewalls, while if maxima and minima were found it would show that the current was confined between those peaks.

As shown in Figure 19, the axial magnetic field distribution at 2.9 cm from the gas injection slit showed well defined maxima and minima. These features were not observed at 1.6 cm and it is possible that current was flowing on the glass sidewalls at that location. Figure 20 shows that a sharply peaked maximum in the axial variation of the same magnetic field component occurred close to the 2.9 cm position. Since this corresponded to the location of the epoxy-fiberglass plate to which the channel was attached (Figure 9) it was felt that ablation was the cause of the spuriously high values of the measured impulse.

Inspection showed extensive charring of the plate had occurred. To check this possibility further, the plasma momentum was measured with the ballistic pendulum suspended inside the vacuum chamber. The result, shown in Figure 21, indicates good agreement between the magnet impulse and the plasma impulse. This seemed to show that there could not have been appreciable current flowing on the glass sidewalls.

Four glass plates were attached to the inner surfaces of the accelerator that covered the plate and electrodes except for the first 1.3 cm downstream from the apex. This modification isolated the epoxy fiberglass plate from the discharge and prevented further ablation from



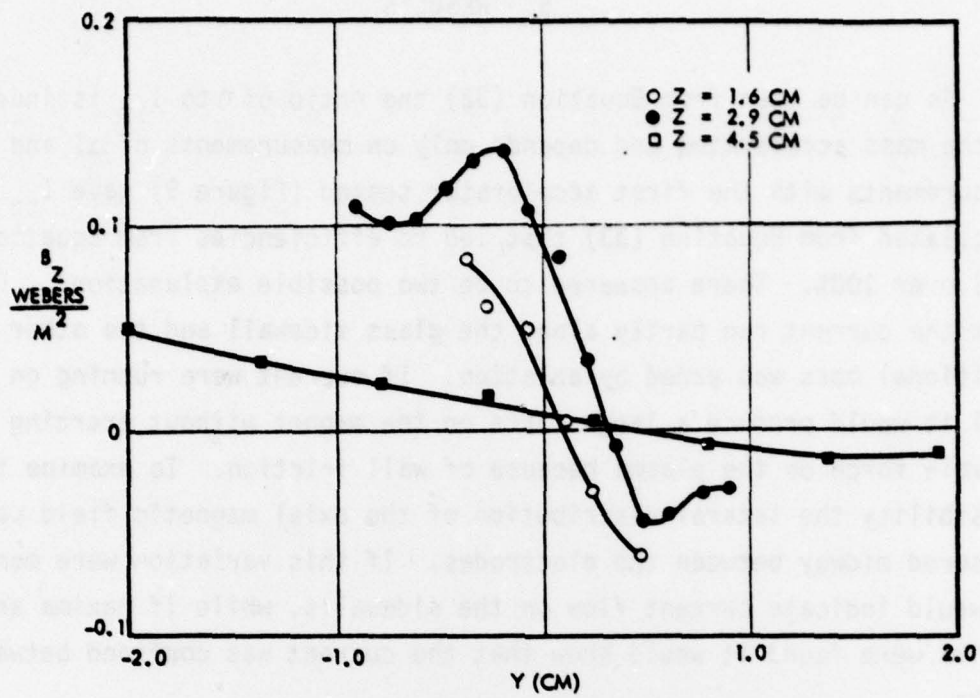


Figure 19. Lateral Variation of Axial Magnetic Field  
(No Glass Covers)

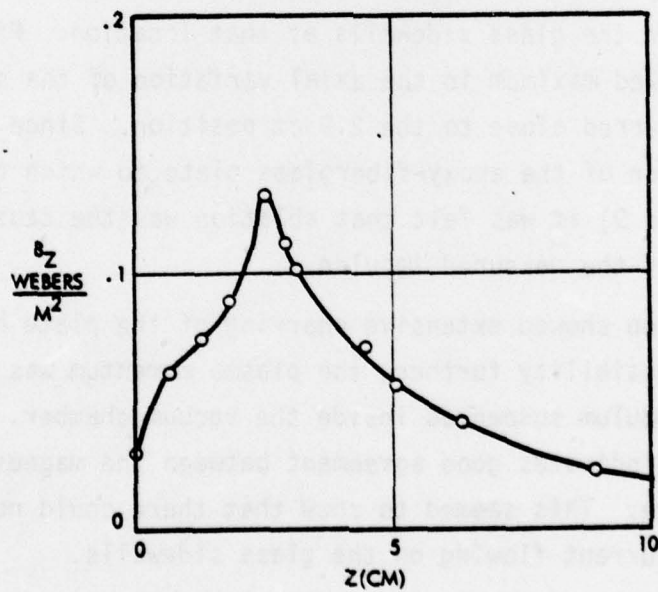


Figure 20. Axial Variation of Axial Magnetic  
Field at Side Wall



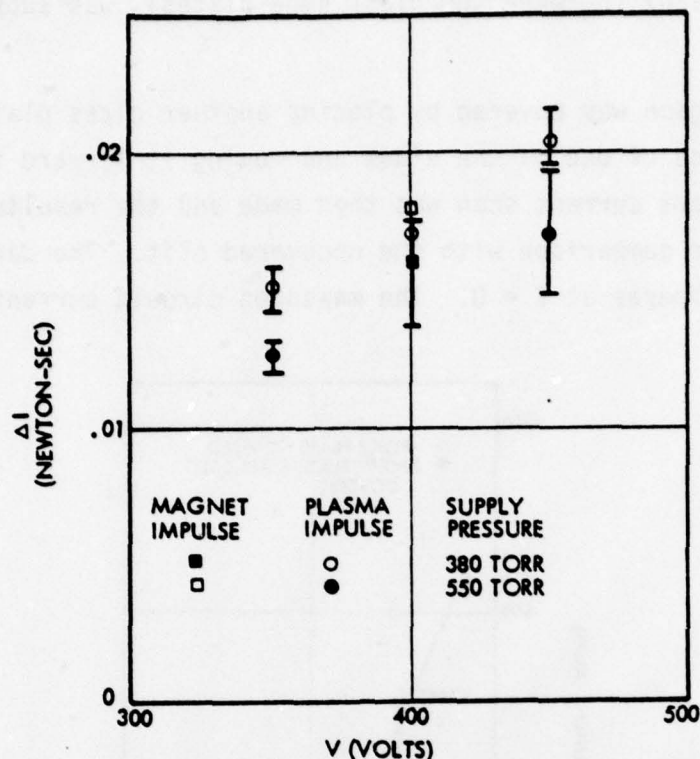


Figure 21. Comparison of Magnet Impulse and Plasma Impulse Measurements

that source. At the same time the sonic slit was closed and gas injection was moved to a pair of 1/8-inch holes in the upper and lower electrodes. This change was made to simplify the gas supply system. Efficiencies greater than 100% were again observed indicating that spurious mass addition must still be occurring.

To obtain a more direct location of the plasma current, a miniature Rogowsky probe was used.

It was roughly rectangular in shape with 5 cm long sides spaced 0.5 cm apart; the long dimension was in the axial direction. An axial scan of the total current passing through the probe window is plotted in Figure 22. It can be seen that no current was running forward of the 1 cm position, i.e., the measured current remained constant to that axial station. It then decreased rapidly, falling to 20% at 2 cm. This indicated that the plasma current was concentrated in a layer a few mm wide at about 1 cm from the apex. It was suspected that epoxy, that was used to seal the

slit at the apex (between the glass side plates), was supplying mass by ablation.

This region was covered by placing another glass plate against the inside surface of one of the sides and moving it forward to close off the slit. A plasma current scan was then made and the results are plotted in Figure 22 for comparison with the uncovered slit. The data extrapolate to about 1000 amperes at  $Z = 0$ . The measured circuit current for this test

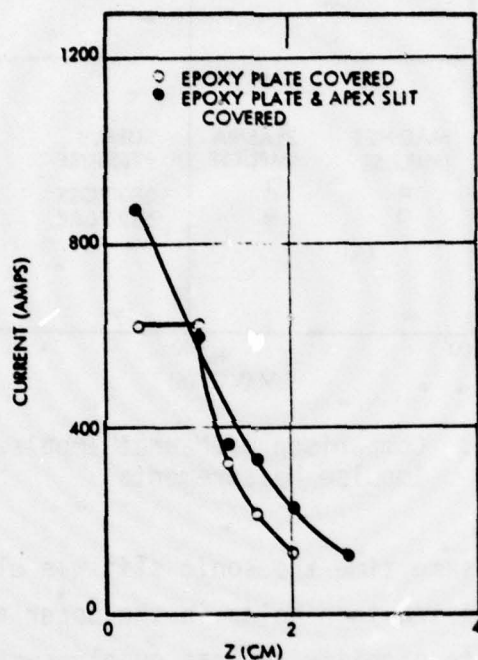


Figure 22. Axial Variation of Current in Rogowsky Probe (450 volts)

was 3200 amperes. Since the probe area covered about one third of the current-carrying cross section, the probe measurement appeared to indicate that the current density was roughly constant.

After several hundred firings of the glass sidewall thruster, with the modification described, it was found that the glass had been ablated by discharges originating near the downstream edges of the large brass electrodes. This showed that more care would have to be taken to reduce ablation, and work on the nearly completed model shown in Figure 23 was terminated. This thruster was built with a long, narrow plenum to permit



Figure 23. Glass Side-Wall Axial Injection Thruster  
Designed for Reduced Ablation

axial gas injection between the closely spaced magnet pole pieces. But it also used brass upper and lower electrode surfaces.

An all-ceramic thruster channel was then built which used sonic gas injection through copper tubes inserted in the upper and lower ceramic plates.

The initial tests with this model showed the same unrealistically large impulse values that had been seen with the glass sidewall thrusters. Because of the clean design, this was not thought to be caused by ablation. A partial explanation appeared to be the interaction between the current flowing in the electrodes and current leads and the fringing magnetic fields above and below the magnet pole pieces. This possibility was examined experimentally by conducting the current between the electrodes in a manner that avoided the magnet field. This was done by attaching copper straps to the electrodes inside the channel and extending them downstream, parallel to the thruster axis for a distance of about 18 inches before crossing the electrode gap.



The magnet deflection was found to be nearly equal to that observed in normal thruster operation. To eliminate this effect, the current was returned through a conductor placed between the pole pieces and the magnet blocks at a location such that no magnet swing was observed when the capacitors were discharged. This conductor can be seen in Figure 11.

The thruster was then operated in its normal mode and very little magnet swing was observed. This indicated that the results achieved with the glass sidewall model, using upper and lower surface gas injection may have been spurious. Evidently the impulse delivered to the magnet had been due to the interaction of the lead current with the fringing magnetic field while the plasma impulse measured by the ballistic pendulum inside the vacuum chamber was due largely to the ablated mass. Thus these impulse values were produced by different mechanisms (both of which were spurious) and the good agreement in the magnitude of the effects was fortuitous.

As shown in Figures 24 and 25, substantial ablation was also encountered with this model. Figure 24 is a close-up view of one of the gas injection/electrode tubes while Figure 25 shows the build-up of ablated material that developed on all four of the channel surfaces. Because of the color of this material it was thought to be copper only.

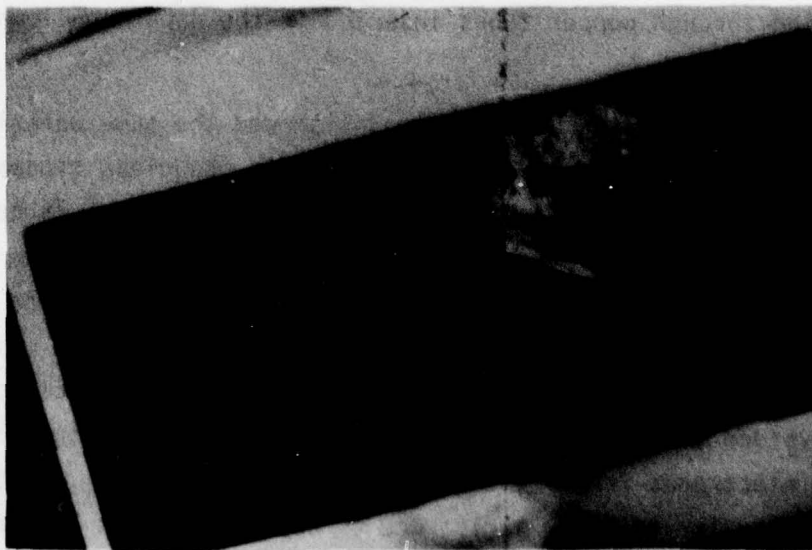


Figure 24. Erosion of Copper Gas Inlet/Electrode in Ceramic Model

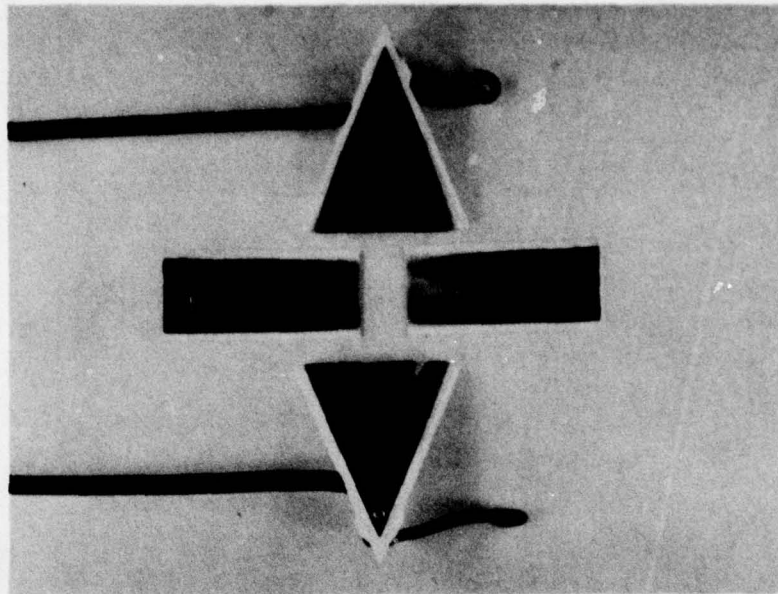


Figure 25. Ablated Material on Inner Surfaces of Ceramic Model with Copper Gas Inlet/Electrodes

At this point it was suspected that the failure of the channel to produce thrust was the result of the method of gas injection. The colliding flow between the hollow electrodes stagnated at hypersonic speeds such that a pressure of several torr resulted. This pressure was too high for a low resistance discharge so that the current would tend to flow well downstream of the bias magnet field. A self-field acceleration would occur in this discharge, but no impulse would be delivered to the magnet. To overcome this difficulty, and hopefully reduce the electrode ablation, the thruster shown in Figure 11 was built. This also used ceramic walls for all surfaces but the electrodes were solid and made of tungsten. As with the first model tested, gas injection was through a sonic slit about 0.05 mm wide.

Again large magnet impulse measurements were made, indicating more than 100% efficiency at low, but reasonable, argon flow rates. After about 100 shots the ablation pattern shown in Figure 26 was seen. The material was black and was thought to be tungsten. The extensive melting of the anode shown in Figure 26 seemed to support this view. One additional attempt was

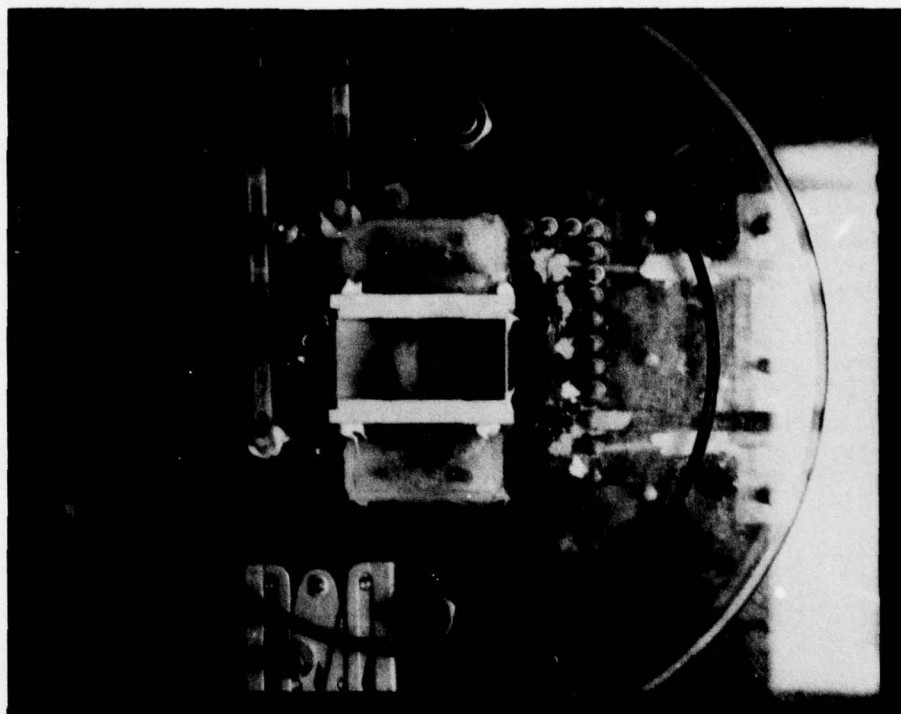


Figure 26. Ablation in Ceramic Thruster with Tungsten Electrodes

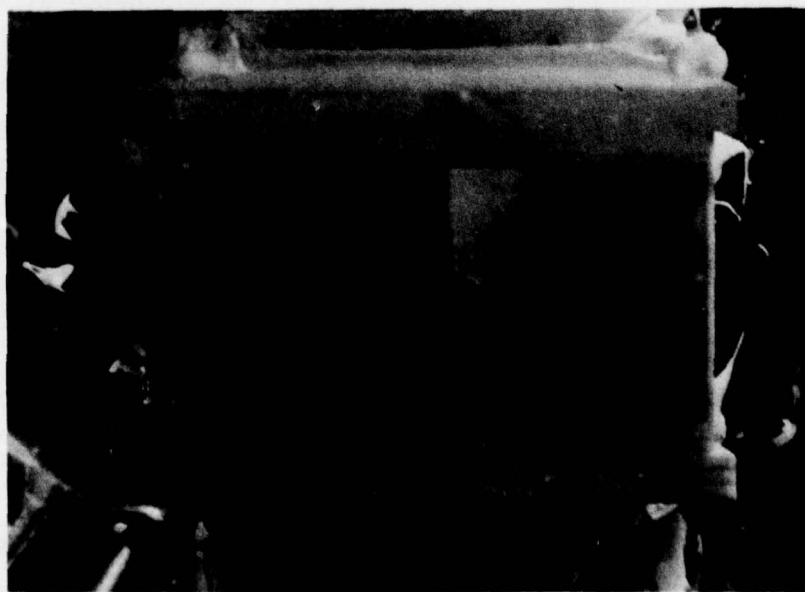


Figure 27. Tungsten Anode Ablation



made to stabilize the current in the bias field region by placing a ceramic rod between the electrodes as shown in Figure 28. After several discharges, with no significant change in performance, the ablation shown in Figure 29 was found. Not shown in this figure is a severe erosion of the leading edge of the rod. Examination of this surface, and the walls, with a microscope showed that much of the ablated material was alumina. The ceramic surfaces resembled a lava flow.

The fact that large magnet impulse values were measured for both the open channel and the ceramic rod (flame arrester) configuration indicates that substantial upstream current must flow, presumably in the sidewall boundary layers and carried by the ablated alumina. The ablation pattern in Figure 27 supports this interpretation.

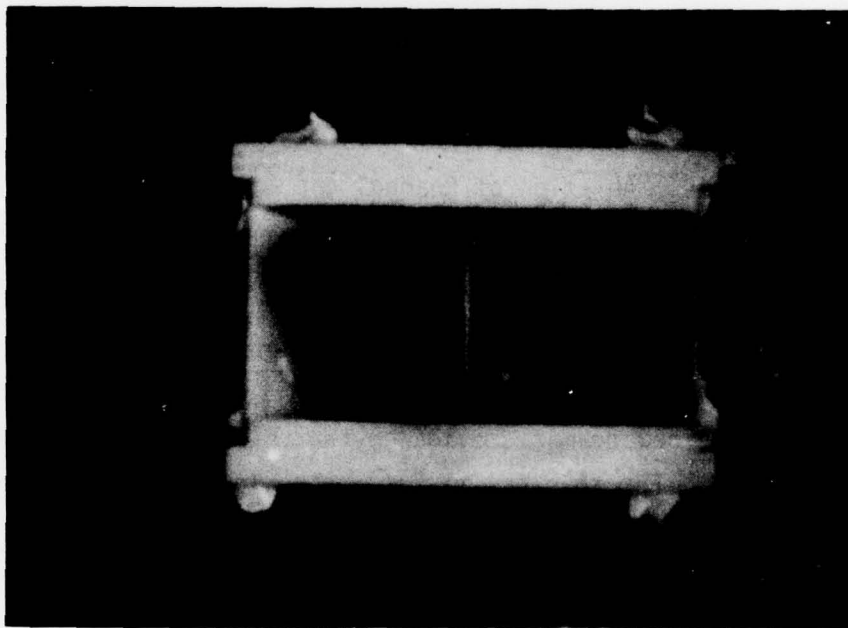


Figure 28. Ceramic Rod "Flame Holder" Before Testing

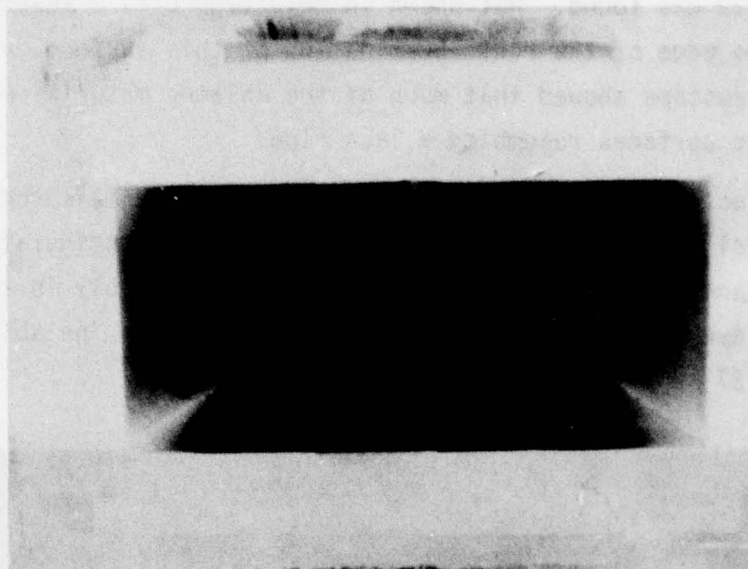


Figure 29. Ablation of Channel and Anode After Testing Ceramic Rod "Flame Holder"

With this result, it was decided that the high power densities for this mode of operation preclude the development of a practical thruster. One further test, made with a mixture of nitrogen and hydrogen ( $N_2 + 2 H_2$ ) provided dramatic evidence that bias field thrust augmentation is not feasible. For this gas mixture, the radiation power density was evidently too low to produce ablation and no magnet deflection was observed.

## 6. CONCLUSIONS .

1. Theoretical calculations of efficiency for the bias field thruster indicate large performance gains relative to self-field thrusters.
2. In the absence of ablation, using a mixture of nitrogen and hydrogen gases ( $N_2 + 2 H_2$ ) the plasma current could not be stabilized in the region of the bias field so that no impulse gain due to the bias field was obtained.
3. With argon, substantial ablation of the alumina channel and tungsten electrodes was found to be unavoidable.
4. It is concluded that a practical bias field thruster is not feasible.